

1 Pre-print Statement for

2 **“Fe₅S₂ identified as a host for sulfur in Earth’s core”**

3 **Claire C. Zurkowski^{a,†}, Barbara Lavina^{b,c}, Abigail Case^a, Kellie Swadba^a, Stella Chariton^b,**
4 **Vitali B. Prakapenka^b, Andrew J. Campbell^a**

5
6 ^aThe University of Chicago, Department of the Geophysical Sciences, 5734 S Ellis Ave, Chicago, IL 60637, USA

7 ^bCenter for Advanced Radiation Sources, The University of Chicago, 9700 South Cass Avenue, Lemont, IL 60439,
8 USA

9 ^cX-ray Science Division, Advanced Photon Source, Argonne National Laboratory, Lemont, IL 60439, USA

10 [†]Now at Earth and Planets Laboratory, Carnegie Institution for Science, 5251 Broad Branch Road, NW,
11 Washington, DC 20015, USA

12
13
14 Corresponding Author: Claire Zurkowski, czurkowski@carnegiescience.edu

15
16
17
18
19 This manuscript is a non-peer reviewed preprint submitted to *EarthArXiv*.
20
21

22
23
24
25
26
27
28
29
30
31
32
33

Fe₅S₂ identified as a host for sulfur in Earth's core

Claire C. Zurkowski^a †, Barbara Lavina^{b,c}, Abigail Case^a, Kellie Swadba^a, Stella Chariton^b,
Vitali B. Prakapenka^b, Andrew J. Campbell^a

^aThe University of Chicago, Department of the Geophysical Sciences, 5734 S Ellis Ave, Chicago, IL 60637, USA

^bCenter for Advanced Radiation Sources, The University of Chicago, 9700 South Cass Avenue, Lemont, IL 60439,
USA

^cX-ray Science Division, Advanced Photon Source, Argonne National Laboratory, Lemont, IL 60439, USA

†Now at Earth and Planets Laboratory, Carnegie Institution for Science, 5251 Broad Branch Road, NW,
Washington, DC 20015, USA

Corresponding Author: Claire Zurkowski, czurkowski@carnegiescience.edu

Abstract

Planetary habitability, as we experience on Earth, is linked to a functioning geodynamo which is in part driven by the crystallization of the liquid iron-nickel-alloy core as a planet cools over time. Cosmochemical considerations suggest that sulfur is a candidate light alloying element in rocky planetary cores of varying sizes and oxidation states; such that, iron sulfide phase relations at extreme conditions contribute to outer core thermochemical convection and inner core crystallization in a wide range of planetary bodies. Here we experimentally investigate the structural properties of the Fe-S system and report the discovery of the sulfide, Fe₅S₂, crystallizing in equilibrium with iron at Earth's outer core pressures and high temperatures. Using single-crystal X-ray diffraction techniques, Fe₅S₂ was determined to adopt the complex Ni₅As₂-type structure ($P6_3cm$, $Z = 6$). These results conclude that Fe₅S₂ is likely to crystallize at the interface of Earth's core and mantle and will begin to crystallize during the freezing out of Earth and Venus' core overtime. The increased metal-metal bonding measured in Fe₅S₂ compared to the other high P - T iron sulfides may contribute to signatures of higher conductivity from regions of Fe₅S₂ crystallization. Fe₅S₂ could serve as a host for Ni and Si as has been

63 observed in the related meteoritic phase, perryite, $(\text{Fe, Ni})_8(\text{P, Si})_3$, adding intricacies to
64 elemental partitioning during inner core crystallization. The stability of Fe_5S_2 presented here is
65 key to understanding the role of sulfur in the multicomponent crystallization sequences that drive
66 the geodynamics and dictate the structures of Earth and rocky planetary cores.

67

68 **Introduction**

69 Earth and the other terrestrial planets along with rocky exoplanets that continue to be
70 discovered are composed of silicate mantles and iron-rich metallic cores (e.g. Birch 1952; Scott
71 and Wasson 1975; Jephcoat and Olsen 1987; McDonough and Sun 1995; Rubie et al. 2011). The
72 likelihood of planetary habitability as we know it demands the presence of a geomagnetic field,
73 sustained by a convecting metallic liquid core, that protects the planet from harmful cosmic rays
74 (e.g. Buffet, 2000). In Earth's liquid outer core, the presence of light alloying elements
75 introduces complex pressure-temperature-dependent melting and crystallization thermodynamics
76 that drives core convection (Fearn and Loper, 1981; Stevenson 1981; 1988; Nimmo 2015).

77 While there remains no method to directly sample Earth's or any terrestrial planetary core, iron
78 meteorites are recognized as relics of the cores of planetesimal building blocks of terrestrial
79 planets, and have long provided insight into the cosmochemically abundant light elements
80 contributing to planetary core dynamics (e.g. Scott and Wasson 1975; Malvin et al. 1984). Of the
81 candidate core-alloying elements such as Si, O, S, C, and H, sulfur is present in nearly all iron
82 meteorites, suggesting that sulfur is a core alloying element in rocky planets with varying sizes,
83 oxidation states, and formation histories (Scott and Wasson 1975; Jones and Drake, 1983;
84 Kruijer et al. 2014). Examination of the structural properties of iron sulfides at high pressures

85 and temperatures (P - T) is therefore critical to ascertaining the chemistry and thermodynamics of
86 Earth, terrestrial and exoplanetary cores.

87 At present, the crystallographic assessment of iron sulfides at Earth and planetary core
88 conditions remains limited, even though properties such as density and elasticity are directly
89 related to the atomic arrangement of core-crystallizing phases and are critical for assessing the
90 seismic and dynamic observations of planetary cores. Previous work on Fe-rich systems indicate
91 that tetragonal Fe_3S (Fe_3P -type structure) is stable from Martian core conditions to Earth's outer
92 core conditions (Fei et al. 2000; Kamada et al. 2010; Ozawa et al. 2013; Mori et al. 2017), and an
93 orthorhombic Fe_2S (Co_2Si -type structure) phase becomes stable near Earth's inner-core boundary
94 (ICB) conditions (Tateno et al. 2019). The presence of Si has also been observed to stabilize the
95 $\text{Fe}_2(\text{S}, \text{Si})$ chemistry over Fe_3S at Mercurian core-mantle-boundary (CMB) conditions (Tao and
96 Fei 2021). These reports were predominantly based powder X-ray diffraction studies at high
97 pressures and temperatures and chemical analyses of recovered samples. However, recent work
98 has demonstrated that the iron-sulfur phase diagram is more complex at high P - T , but that this
99 complexity requires a superior method for accurately characterizing crystal structures at extreme
100 conditions. Using single-crystal X-ray diffraction techniques on multigrain samples, Co_2P -type
101 Fe_2S ($Pnma$, $Z = 4$) was recently identified and characterized at 90 GPa (Zurkowski et al. *in*
102 *press*). It remains, however, that these methods have not been applied to iron-sulfide phases
103 synthesized at high temperatures above 90 GPa, leaving the role of sulfur in the crystallization
104 sequences occurring in Venus, Earth and larger rocky exoplanets open to further discovery.

105

106

107 **Results and Discussion**

108 In the current study, Fe-rich Fe-S compositions were probed using both single-crystal and
109 powder X-ray diffraction techniques in a laser-heated diamond anvil cell to 200 GPa and 3300 K.
110 At high temperatures between 120 and 200 GPa, spanning Earth's CMB to mid-outer-core
111 conditions, crystallization of hcp-Fe (Figure 1a) is observed in the diffraction patterns along with
112 diffuse streaks and sets of closely spaced reciprocal nodes (Figure 1a, Figure S1), suggesting a
113 complex atomic arrangement of the coexisting sulfide. Upon temperature quenching in this
114 pressure range, diffraction images were collected while rotating the DAC across a +/- 17–30°
115 range (depending on the DAC configuration). Grains of a hexagonal lattice were identified in the
116 reciprocal space with indexed parameters: $a = 5.979(3) \text{ \AA}$, $11.088(6) \text{ \AA}$ at 140(2) GPa and
117 3070(180) K (Table S1). Assessment of the systematic absences for the structure factors reduced
118 for this hexagonal sulfide suggests a $P6_3cm$ space group, and structural solution and positional
119 and displacement parameter refinement converged to the Ni_5As_2 -type Fe_5S_2 ($Z=6$) (Table S2, S3;
120 Figure 2) (Oryshchyn et al. 2011). The Ni_5As_2 -type Fe_5S_2 is derived from the Pb_5Sb_2 structure
121 (El-Boragy et al. 1970) where the Fe6 site (Table S3) is split about its position and given half
122 occupancy, changing its Wyckoff site from $6c$ to $12d$ (Oryshchyn et al. 2011) (Figure 2, Table
123 S3, Appendix A1). Within error, all sites are fully occupied, except the Fe6 site that is ascribed
124 half occupancy (Oryshchyn et al. 2011).

125 Additionally, two polytypes associated with stacking variations along the c direction were
126 measured at lower temperatures and in stiff pressure media (Table S1). The Fe_5S_2 polytypism is
127 accompanied by observations of diffuse scattering between reciprocal nodes along the c direction
128 (Figure S1), indicating positional disorder as the atoms configure at high temperatures.
129 Analogous polytypes have been reported in related phases such as Pb_5Sb_2 (Saini et al. 1964).

130 X-ray diffraction from seven heating cycles performed between 100 and 200 GPa and to
131 3300 K provide insight into the Fe-rich Fe-S phase relations at outer core pressures and to high
132 temperatures. In each heating experiment, temperatures near melting were attained, and lattices
133 of Fe₅S₂ were indexed in the reciprocal space upon quenching. By further probing locations
134 across the thermal gradient of the laser heated spots, additional Fe-sulfides were characterized,
135 offering information on the lower temperature Fe-saturated sulfide crystal chemistries (Table S1,
136 S2). These include the Fe₃P-type Fe₃S (*I*-4, *Z* = 8) phase (Fei et al. 2000; Seagle et al. 2006;
137 Morard et al. 2007; Kamada et al. 2010; Kamada et al. 2012; Thompson et al. 2020), the *C*23
138 Fe₂S (*Co*₂P-type, *Pnma*, *Z* = 4) phase, and the *C*37 Fe₂S (*Co*₂Si-type, *Pnma*, *Z*=4) phase, in lower
139 temperature regions at 119 GPa, 131 GPa, and 140 GPa, respectively (Figure 3; Table S1, S2).
140 Notably, identification and crystal-structure analysis of Fe₅S₂ and Fe₃S in these Fe-saturated
141 experiments clarifies that Fe₅S₂, not Fe₃S is stable on the solidus above 120 GPa, despite reports
142 from previous powder diffraction studies (e.g. Kamada et al. 2010; Kamada et al. 2012; Ozawa
143 et al. 2013; Mori et al. 2017).

144 Comparison of the interatomic distances and coordination environments in the Fe-
145 sulfides observed in this study separates Fe₅S₂ as particularly unique among them. Within an
146 interatomic distance of 2.7 Å (Table S4, Appendix A1-A4), *C*23 and *C*37 Fe₂S consist of Fe sites
147 coordinated only by S, Fe₃S marks an increase in Fe-Fe bonding with Fe surrounded by up to 9
148 Fe sites, and Fe₅S₂ exhibits Fe surrounded by up to 9 Fe sites with Fe-Fe bond lengths up to 25%
149 shorter in Fe₅S₂ compared to Fe₃S (Table S4). Following previous descriptions of related *M*₅*X*₂
150 phases (e.g. (Kjekshus et al. 1973; Oryshchyn et al. 2011), Fe₅S₂ can be viewed as an
151 arrangement of 6 Fe sites and 3 S sites with the Fe1, Fe2, Fe4, and Fe6 sites in 13-fold

152 coordination, the Fe3 and Fe5 sites in 12-fold coordination, and the S sites in 10-fold
153 coordination (Figure 2c, Table S4). All sites are coordinated by both Fe and S sites.

154 The presented single-crystal derived structures of Fe_5S_2 , Fe_3S , $C23 \text{Fe}_2\text{S}$, and $C37 \text{Fe}_2\text{S}$
155 were then used to interpret the changes in powder X-ray diffraction patterns collected during
156 heating between 110 and 200 GPa and to ~ 3300 K (Figure 4, Figure S4). $C23 \text{Fe}_2\text{S}$ is observed
157 coexisting with Fe to ~ 125 GPa and up to ~ 2300 K. In combination with previous studies, $C23$
158 Fe_2S is stable at moderate temperatures between 25 and 125 GPa (Zurkowski et al. *in press*,
159 Zurkowski et al. submitted). A pressure-induced $C23$ – $C37 \text{Fe}_2\text{S}$ transition is constrained between
160 125 and 135 GPa, in agreement with previous investigations of Fe_2S (Zurkowski et al.
161 submitted). $C37 \text{Fe}_2\text{S}$ is stable between 130–200 GPa and to ~ 3000 K in this study, and previous
162 work suggests that $C37 \text{Fe}_2\text{S}$ may remain stable to 306 GPa at high temperatures (Tateno et al.
163 2019). Tetragonal Fe_3S forms from the reaction of $C23 \text{Fe}_2\text{S} + \text{Fe}$ between 2000–2400 K at ~ 115
164 GPa. The stability of tetragonal Fe_3S is constrained to pressures below ~ 120 GPa at high
165 temperatures in Fe-rich systems (Figure 4) (Seagle et al. 2006; Morard et al. 2008; Kamada et al.
166 2010; Kamada et al. 2012; Thompson et al, 2020). Fe_5S_2 is observed coexisting with iron
167 between ~ 120 – 200 GPa and in the 2400–3300 K range, making it the relevant sulfide in the
168 melting and crystallization properties of Fe-rich metallic cores at these pressures (Figure 4).

169 **Sulfur in Earth and planetary cores**

170 The stability of Fe_5S_2 and the phase relations observed in this study present novel
171 constraints on the material properties of Fe-sulfides at conditions relevant to Earth's outer core,
172 Venus' core, and exoplanetary cores of similar size and core-mass fraction (CMF). Namely, at
173 pressures ≥ 120 GPa, Ni_5As_2 -type Fe_5S_2 , not tetragonal Fe_3S as previously believed, is the

174 relevant Fe-rich sulfide. As Earth's outer core crystallizes over time, Fe_5S_2 will eventually
175 crystallize over a large depth range up to the CMB. Tetragonal Fe_3S has been confirmed up to
176 120 GPa (Figure 4) (Seagle et al. 2006; Morard et al. 2008; Thompson et al., 2020), constraining
177 the $\text{Fe}_3\text{S} + \text{Fe} \rightarrow \text{Fe}_5\text{S}_2 + \text{Fe}$ transition to ~ 120 GPa. Rocky planetary bodies with sizes and CMFs
178 like that of Venus (CMB = 114 GPa) (Aitta 2012) would likely crystallize Fe_3S at the CMB,
179 while Fe_5S_2 will be crystallizing over much of the core's depth. $C37$ Fe_2S is reported to be stable
180 on the solidus above 306 GPa in Fe-rich systems (Tateno et al. 2019), suggesting a $\text{Fe}_5\text{S}_2 + \text{Fe} \rightarrow$
181 $\text{Fe}_2\text{S} + \text{Fe}$ transition in the 200–300 GPa range. $C37$ Fe_2S remains the candidate Fe-rich sulfide
182 at Earth's ICB, but for planets like Venus with a central pressure of 274 GPa (Aitta 2012), Fe_5S_2
183 may instead be the relevant Fe-rich sulfide, necessitating experimental determination of the
184 $\text{Fe}_5\text{S}_2 \rightarrow \text{Fe}_2\text{S} + \text{Fe}$ decomposition P - T boundary. Additional assessment of the volume and
185 melting-temperature changes across these newly determined sulfide transitions are critical for
186 matching the density and seismic profiles of Earth and rocky planetary cores. Furthermore, as
187 Fe_5S_2 exhibits a complex crystalline arrangement with significant metal-metal bonding compared
188 to Fe_2S and Fe_3S at core pressures, the significant depth over which Fe_5S_2 crystallizes in and
189 Venus- to Earth-sized planetary cores is likely to contribute to higher conductivity signatures in
190 these regions.

191 Terrestrial core chemistries are multicomponent; Si and Ni are also important core-
192 alloying elements in planets such as Earth, drawing attention to the potential stability of the
193 perryite $(\text{Fe}, \text{Ni})_8(\text{Si}, \text{P})_3$ structure in $(\text{Fe}, \text{Ni}) - (\text{Si}, \text{S})$ -rich cores. Perryite, is a mineral observed
194 in enstatite chondrites and aubrites that adopts a structure that is trigonal stacking variant of the
195 Ni_5As_2 -type structure (Wasson and Wai, 1970; Okada et al. 1991) and iron phosphides tend to
196 adopt analogous structures to that observed in iron sulfides (i.e., Fei et al. 2000; Dera et al. 2008;

197 Gu et al. 2014; Gu et al. 2016; Zurkowski et al., in press). Fe_5S_2 could potentially serve as a host
198 for nickel and silicon in the perryite structure at Earth's outer core conditions. Further, Si has
199 recently been shown to dissolve into iron-sulfide phases and expand their stability fields with
200 pressure (Tao and Fei, 2021). The dissolution of silicon into Fe_5S_2 may expand its stability to
201 higher pressures, making it potentially relevant at Earth's ICB conditions. If this is the case, the
202 partitioning of Si and Ni between $(\text{Fe}, \text{Ni})_5(\text{S}, \text{Si})_2$ and $(\text{Fe}, \text{Ni}, \text{Si})$ and the density difference
203 between the inner-core-crystallizing phase and remaining light-element-rich liquid will be crucial
204 to investigations of the inner-core-density deficit and inner core seismic morphology.

205

206 **Materials and Methods**

207 Experiments targeting multigrain synthesis in the Fe-S system consisted of mixtures of Fe
208 (99.9+%, <10 μm , Alfa Aesar) and iron sulfide (FeS , 99.99%, Alfa Aesar) in Fe+12.5 wt% S
209 ($\text{Fe}_{80}\text{S}_{20}$), Fe + 23 wt% S ($\text{Fe}_{67}\text{S}_{33}$) compositions. The Fe-FeS compositions were ground in
210 ethanol in a pestle and mortar for 1 hour then mixed dry for a short interval to homogenize any
211 density settling during alcohol evaporation.

212 Pressure was generated using BX-90-type (Kantor et al. 2012) diamond anvil cells (DAC)
213 with type 1 Boehler-Almax conical diamonds and seats, and Mao symmetric-type DACs with
214 Type 1 standard cut diamonds mounted on tungsten carbide or cubic-boron nitride (cBN) seats.
215 Diamond culets ranged from 150-50 μm in diameter. Foils of $\text{Fe}_{80}\text{S}_{20}$ or $\text{Fe}_{67}\text{S}_{33}$ were produced
216 by pressing the Fe-S starting powders between two ungasketed diamond anvils, then loaded
217 between pellets of KCl or SiO_2 . Sample chambers ranged from 180-25 μm in diameter and were
218 drilled from pre-indented rhenium gaskets. Samples were dried at 100°C for 30 minutes prior to
219 pressurization.

220 Angle dispersive X-ray diffraction (XRD) experiments were conducted at Argonne
221 National Laboratory, sector 13 ID-D, of the Advanced Photon Source. At Sector 13 ID-D, a 2.5
222 $\mu\text{m} \times 3.54 \mu\text{m}$ full width, half maximum (FWHM) monochromatic X-ray beam tuned to 37 or 42
223 keV was utilized, and diffracted X-rays were collected with a CdTe 1M Pilatus detector. Sample-
224 to-detector geometries were calibrated using a LaB₆ NIST standard and a single crystal of
225 enstatite was used for calibration of the rotational geometry of the X-ray beam and detector.

226 Double-sided laser heating and *in-situ* XRD collection took place at Sector 13 ID-D. Fibers
227 lasers shaped with $\sim 10 \mu\text{m}$ radius flat tops were aligned with the X-ray beam using the X-ray
228 fluorescence of the sample pressure media or the gasket (Prakapenka et al., 2008). During
229 heating, thermal emission from a $6 \mu\text{m}$ central region of the laser-heated spot was measured
230 spectroradiometrically and fit to a gray body approximation (Heinz and Jeanloz, 1987). A 3%
231 temperature correction was then applied to correct for axial gradients through the sample
232 (Campbell et al., 2007; 2009). The laser power on each side of the sample was adjusted to
233 maintain uniform double-sided heating and X-Ray diffraction and temperature measurements
234 were collected every $\sim 200 \text{ K}$ with 1s exposure times. Samples were typically quenched at high
235 temperatures within 30-45 minutes of heating or after a phase transition and suitable grain
236 growth was observed. Powder diffraction patterns were processed using Dioptas (Prescher and
237 Prakapenka, 2015) and CrysAlisPro (Rigaku OD, 2018). Pressure was determined using the
238 equation of state of hcp-Fe (Dewaele et al. 2006).

239 Upon quenching, X-ray diffraction maps of the heated spot were collected across a 100
240 μm^2 square region in $3 \mu\text{m}$ steps. Map locations showing high intensity, spotty diffraction
241 patterns were chosen for multigrain single-crystal type X-ray diffraction collection approach, as
242 these features indicate high-temperature induced crystallite growth. At chosen map locations, X-

243 ray diffraction images were collected across ± 17 to $\pm 30^\circ$ rotational scans in 0.25° – 0.5° steps with
244 1–4 s exposure times. The diffraction reflections were then mapped in the reciprocal space and
245 target grains were identified and separated from reflections associated with the pressure media,
246 iron, and diamond (Rigaku OD, 2018).

247 Target Fe-S lattices were then indexed and the peak intensities were integrated and reduced
248 using CrysAlisPro (Rigaku OD, 2018). Absorption corrections and scaling factors were applied to
249 the structure factors in CrysAlisPro using the multi-scan method via the Scale3 Abspack program
250 (Rigaku OD, 2018). The final structure factors and lattice geometries were then refined to known
251 structure models (El-Boragy et al. 1970; Oryshchyn et al. 2011) using SHELXL2014/7
252 (Sheldrick 2015). Reflections showing anomalous calculated versus measured structure factors;
253 likely due to overlap with diamond and other phases in the multigrain sample, resolution
254 limitations, and volume of crystal illuminated by the X-ray beam, were omitted. Structure
255 models were visualized using Vesta during the refinement procedure (Momma and Izumi 2011).

256

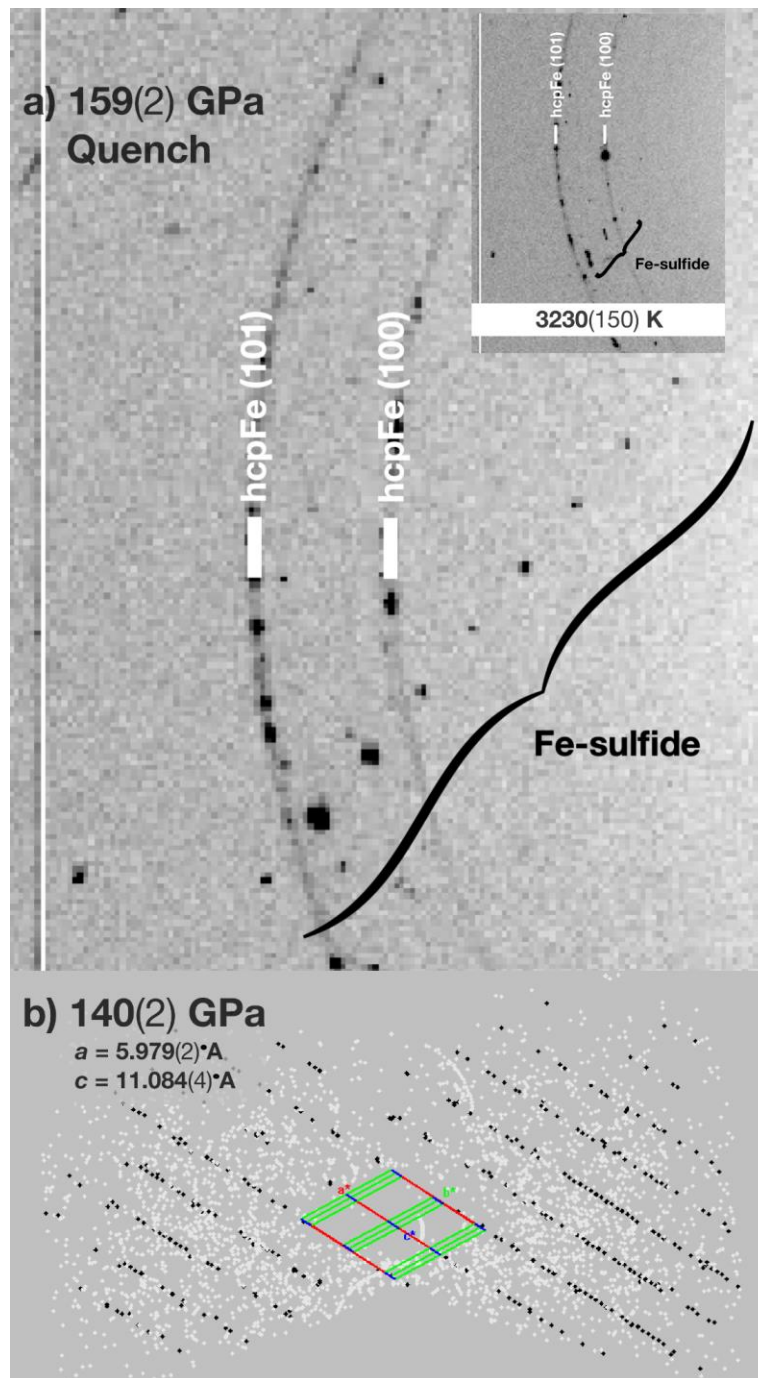
257 **Acknowledgments**

258 Portions of this work were performed at GeoSoilEnviroCARS (The University of Chicago,
259 Sector 13), Advanced Photon Source (APS), Argonne National Laboratory.

260 GeoSoilEnviroCARS is supported by the National Science Foundation - Earth Sciences (EAR -
261 1634415). This research used resources of the Advanced Photon Source, a U.S. Department of
262 Energy (DOE) Office of Science User Facility operated for the DOE Office of Science by
263 Argonne National Laboratory under Contract No. DE-AC02-06CH11357. Use of the
264 COMPRES-GSECARS gas loading system was supported by COMPRES under NSF
265 Cooperative Agreement EAR -1606856 and by GSECARS through NSF grant EAR-1634415

266 and DOE grant DE-FG02-94ER14466. This research used resources of the Advanced Photon
267 Source, a U.S. Department of Energy (DOE) Office of Science User Facility operated for the
268 DOE Office of Science by Argonne National Laboratory under Contract No. DE-AC02-
269 06CH11357. This material is based upon work supported by a National Science Foundation
270 Graduate Research Fellowship to C.C.Z. This work was also supported by the National Science
271 Foundation by grant EAR-1651017 to A.J.C.

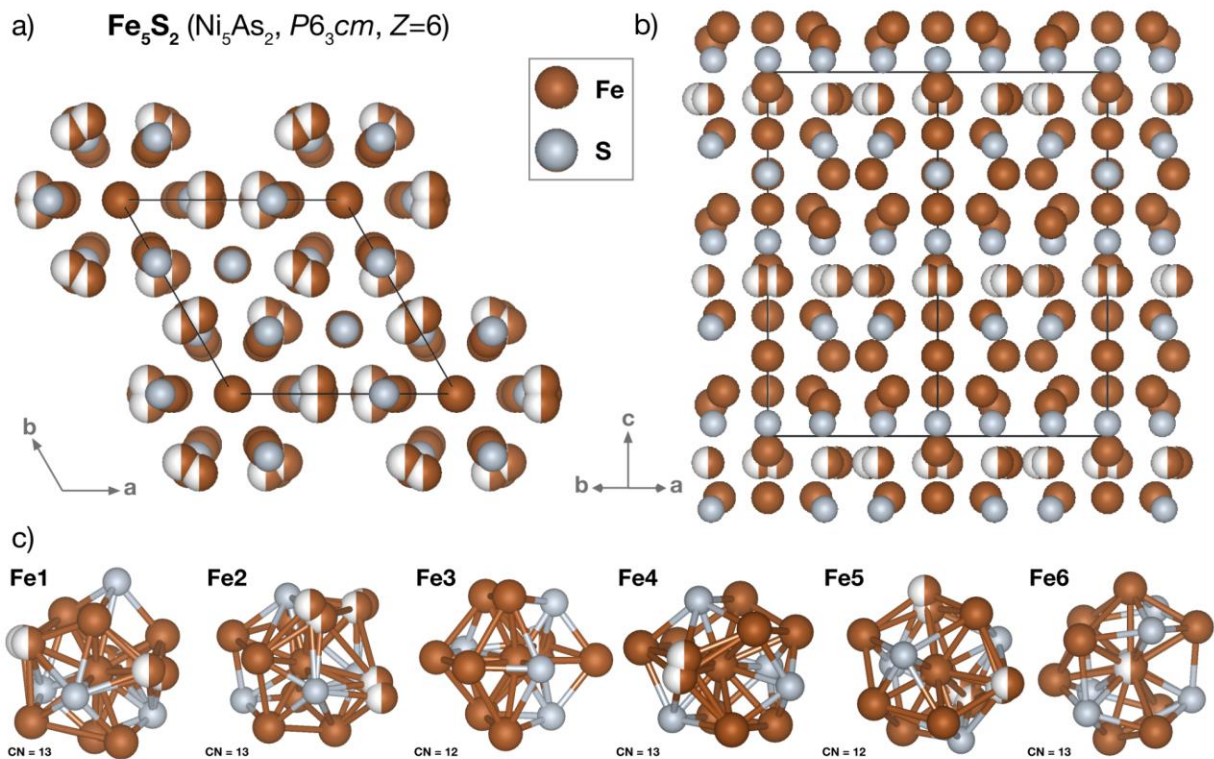
272



274

275 **Figure 1. Fe₅S₂ diffraction in equilibrium with iron**

276 a) View of a crystallite of the high-temperature Fe₅S₂ coexisting with recrystallized hcp-Fe after
 277 synthesis at 159(2) GPa and 3230(130) K (inset). The spotty rings corresponding to the hcp-Fe
 278 (100) and (101) planes demonstrate that iron equilibrated at 159(2) GPa and 3230(130) K. b)
 279 View of the reciprocal space for reflections detected in an experiment on the Fe₈₀S₂₀ composition
 280 quenched from 140(2) GPa and 3070(140) K. The reciprocal lattice, colored in black, is
 281 associated with a Fe₅S₂ grain whose lattice parameters are provided in the top left.



282

283

284

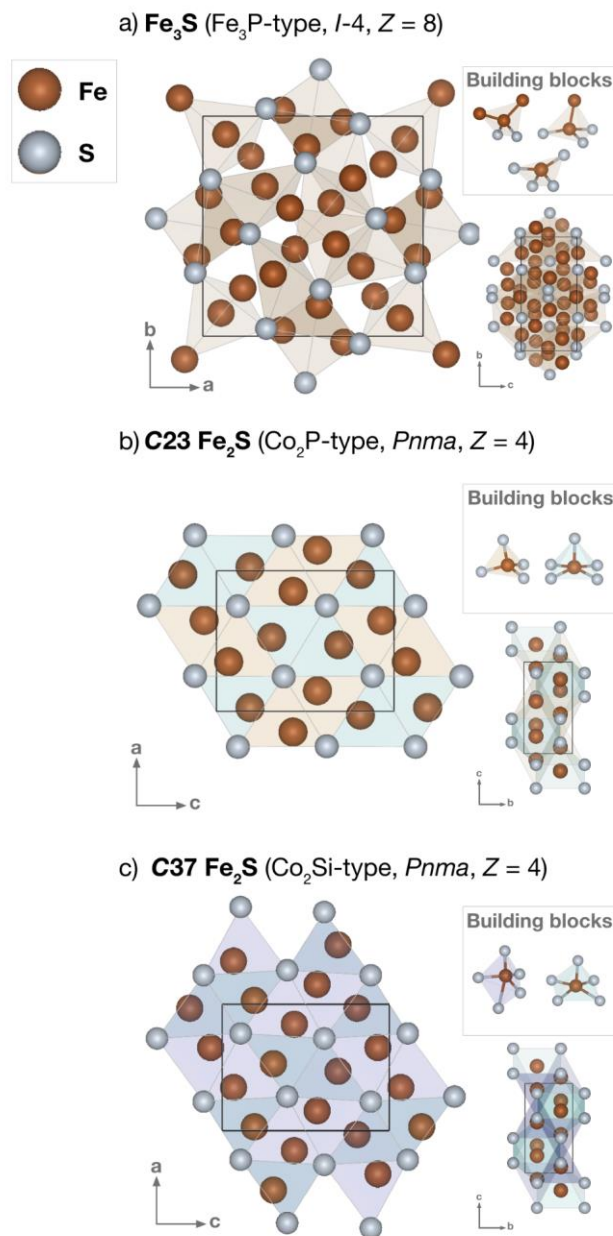
285

286

287

Figure 2. Crystal structure of Ni_5As_2 -type Fe_5S_2

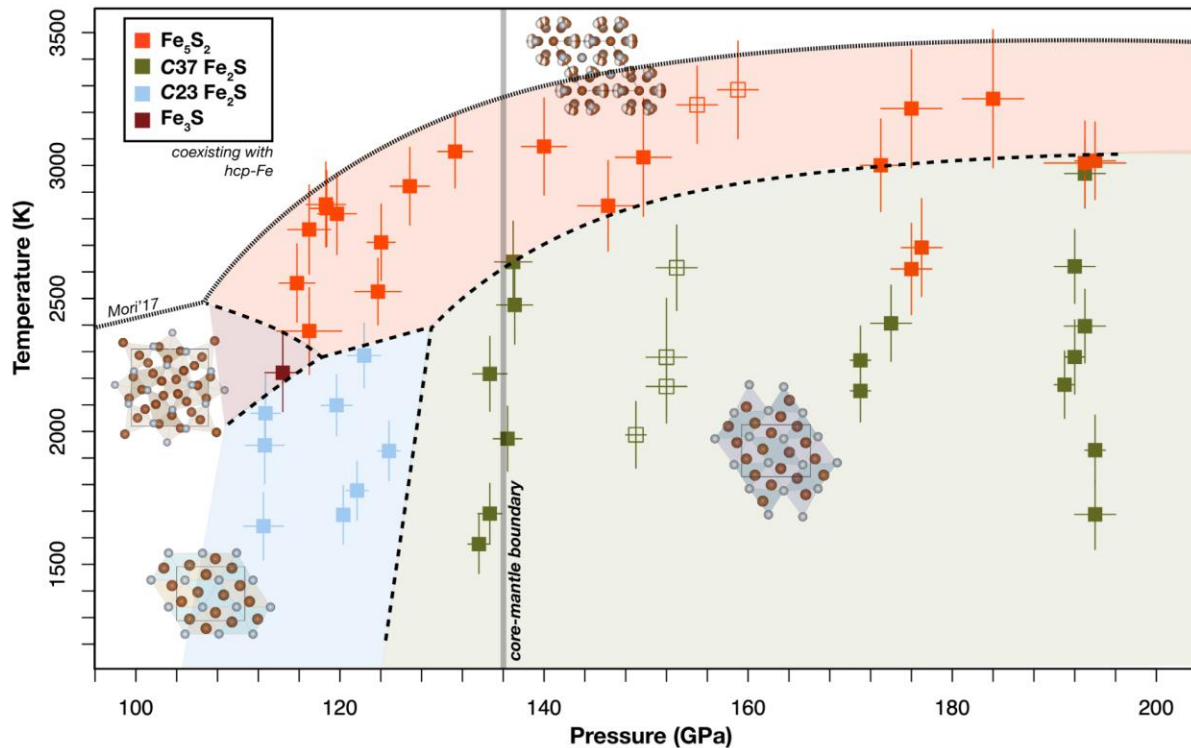
Crystal structure of Fe_5S_2 viewed along the a) c axis and the b) (100) plane. c) The Fe-coordination polyhedra observed in this atomic arrangement are provided. Fe1, Fe2, Fe4, and Fe6 are coordinated by 13 sites and Fe3 and Fe5 are coordinated by 12 sites. Each coordination polyhedron consists of Fe and S sites.



288

289 **Figure 3. Crystal structures of Fe_3S and Fe_2S observed in this study**

290 a) Fe_3S adopts the Fe_3P -type structure ($I-4$, $Z = 8$) that is composed of three tetrahedrally
 291 coordinated Fe-sites, each with increasing Fe–Fe bonding. b) The $\text{C}23 \text{Fe}_2\text{S}$ structure (Co_2P -type,
 292 $Pnma$, $Z = 4$) is made up of columns of FeS_4 tetrahedra and columns of FeS_5 square pyramids
 293 linked along edges in the b direction. c) The $\text{C}37 \text{Fe}_2\text{S}$ structure (Co_2Si -type, $Pnma$, $Z = 4$) has
 294 the same site symmetries as the $\text{C}23$ structure, but is marked by a shortened a axis and elongated
 295 b and c axes accompanied by the formation of a 5-fold dipyramid.



296

297 **Figure 4. Iron-rich sulfide phase diagram to Earth's outer core pressures**

298 At moderate temperatures up to 130 GPa, C23 Fe₂S is observed. At moderate temperatures,
 299 tetragonal Fe₃S (Fe₃P-type) is observed below 120 GPa. At moderate temperatures between 130
 300 and 200 GPa, C37 Fe₂S is observed, and on the liquidus between ~115–200 GPa, Fe₅S₂ is the
 301 liquidus phase. A kink the Fe-S solidus curve (Mori et al. 2017), is presented to account for the
 302 change in phase relations and the high temperatures at which Fe₅S₂ was observed. The closed
 303 squares represent experiments conducted on the Fe₈₀S₂₀ starting material, and the open squares
 304 represent experiments conducted on the Fe₆₇S₃₃ starting material. Both show compatible results,
 305 likely indicating that Fe-rich regions of the Fe₆₇S₃₃ foils were probed.

306

307

308

309

310

311

312

313

314

315 **References**

- 316 Anzellini, S., Dewaele, A., Mezouar, M., Loubeyre, P. and Morard, G. (2013). Melting of iron at
317 Earth's inner core boundary based on fast X-ray diffraction. *Science*, 340, 464–466.
- 318 Birch, F. (1952) Elasticity and constitution of the Earth's interior. *Journal of Geophysical*
319 *Research*, 57, 227–286.
- 320 Buffett, B.A. (2000) Earth's core and the geodynamo. *Science*, 288, pp.2007-2012.
- 321 Campbell, A.J., Seagle, C.T., Heinz, D. L., Shen, G., and Prakapenka, V.B. (2007) Partial
322 melting in the iron-sulfur system at high pressure: A synchrotron X-ray diffraction study.
323 *Physics of the Earth and Planetary Interiors*, 162, 119–128.
- 324 Campbell, A.J., Danielson, L., Righter, K., Seagle, C.T., Wang, Y. and Prakapenka, V.B. (2009)
325 High pressure effects on the iron–iron oxide and nickel–nickel oxide oxygen fugacity
326 buffers. *Earth and Planetary Science Letters*, 286, 556–564.
- 327 Chen, J.H. and Whitmire, K.H. (2018) A structural survey of the binary transition metal
328 phosphides and arsenides of the d-block elements. *Coordination Chemistry Reviews*, 355,
329 271–327.
- 330 Dewaele, A., Loubeyre, P., Occelli, F., Mezouar, M., Dorogokupets, P.I. and Torrent, M. (2006)
331 Quasihydrostatic equation of state of iron above 2 Mbar. *Physical Review Letters*, 97,
332 215504.
- 333 Dziewonski, A.M. and Anderson, D.L. (1981) Preliminary reference Earth model. *Physics of the*
334 *Earth and planetary interiors*, 25, 297–356.
- 335 El-Boragy, M., Bhan, S. and Schubert, K. (1970) Kristallstruktur von Pd₅Sb₂ und Ni₅As₂ und
336 einigen varianten. *Journal of the Less Common Metals*, 22, 445–458.
- 337 Evans, H.T. (1970) Lunar troilite: crystallography. *Science*, 167, 621–623.
- 338 Fearn, D.R. and Loper, D.E., (1981). Compositional convection and stratification of Earth's core.
339 *Nature*, 289, 393–394.
- 340 Fei, Y., Prewitt, C.T., Mao, H.K. and Bertka, C.M (1995). Structure and density of FeS at high
341 pressure and high temperature and the internal structure of Mars. *Science*, 268, 1892–
342 1894.
- 343 Fei, Y., Bertka, C.M. and Finger, L.W. (1997) High-pressure iron-sulfur compound, Fe₃S₂, and
344 melting relations in the Fe–FeS system. *Science*, 275, 1621–1623.
- 345 Fei, Y., Li, J., Bertka, C.M. and Prewitt, C.T. (2000) Structure type and bulk modulus of Fe₃S, a
346 new iron-sulfur compound. *American Mineralogist*, 85, 1830–1833.
- 347 Fei, Y., Ricolleau, A., Frank, M., Mibe, K., Shen, G. and Prakapenka, V. (2007) Toward an
348 internally consistent pressure scale. *Proceedings of the National Academy of Sciences*,
349 104, 9182–9186.
- 350 Frank, K. and Schubert, K. (1971) Kristallstruktur von Ni₃₁Si₁₂. *Acta Crystallographica Section*
351 *B: Structural Crystallography and Crystal Chemistry*, 27, 916–920.
- 352 Heinz, D.L., and Jeanloz, R. (1987) Measurement of the melting curve of Mg_{0.9}Fe_{0.1}SiO₃ at
353 lower mantle conditions and its geophysical implications. *Journal of Geophysical*
354 *Research*, 92, 437–444.

355 Irving, J.C., Cottaar, S. and Lekić, V. (2018) Seismically determined elastic parameters for
356 Earth's outer core. *Science advances*, 4, 2538.

357 Jephcoat, A. and Olson, P., (1987) Is the inner core of the Earth pure iron? *Nature*, 325, 332–
358 335.

359 Jones, J.H. and Drake, M.J. (1983). Experimental investigations of trace element fractionation in
360 iron meteorites, II: The influence of sulfur. *Geochimica et Cosmochimica Acta*, 47,
361 1199–1209.

362 Kamada, S., Terasaki, H., Ohtani, E., Sakai, T., Kikegawa, T., Ohishi, Y., Hirao, N., Sata, N. and
363 Kondo, T. (2010) Phase relationships of the Fe–FeS system in conditions up to the
364 Earth's outer core. *Earth and Planetary Science Letters*, 294, 94–100.

365 Kamada, S., Ohtani, E., Terasaki, H., Sakai, T., Miyahara, M., Ohishi, Y. and Hirao, N. (2012)
366 Melting relationships in the Fe–Fe₃S system up to the outer core conditions. *Earth and*
367 *Planetary Science Letters*, 359, 26–33.

368 Kantor, I., Prakapenka, V., Kantor, A., Dera, P., Kurnosov, A., Sinogeikin, S., Dubrovinskaia, N.
369 and Dubrovinsky, L. (2012) BX90: A new diamond anvil cell design for X-ray
370 diffraction and optical measurements. *Review of Scientific Instruments*, 83, 125102.

371 King, H. and Prewitt, C.T. (1982) High-pressure and high-temperature polymorphism of iron
372 sulfide (FeS). *Acta Crystallographica Section B: Structural Crystallography and Crystal*
373 *Chemistry*, 38, 1877–1887.

374 Kjekshus, A., Skaug, K.E., Hebrew, C., Van Buren, C.T., Klæboe, P. and Swahn, C.G. (1973).
375 On the crystal structure of Ni₅As₂. *Acta Chem. Scand.*, 27, 582–588.

376 Kruijer, T.S., Touboul, M., Fischer-Gödde, M., Bermingham, K.R., Walker, R.J. and Kleine, T.,
377 2014a. Protracted core formation and rapid accretion of protoplanets. *Science*, 344,
378 1150–1154.

379 Kuwayama, Y., Morard, G., Nakajima, Y., Hirose, K., Baron, A.Q., Kawaguchi, S.I., Tsuchiya,
380 T., Ishikawa, D., Hirao, N. and Ohishi, Y. (2020). Equation of state of liquid iron under
381 extreme conditions. *Physical review letters*, 124, .165701.

382 Litasov, K.D., Shatskiy, A.F., Minin, D.A., Kuper, K.E. and Ohfuji, H. (2019). The Ni–Ni₂P
383 phase diagram at 6 GPa with implication to meteorites and super-reduced terrestrial
384 rocks. *High Pressure Research*, 39, 561–578.

385 Maaref, S., Madar, R., Chaudouet, P., Fruchart, R., Senateur, J.P., Averbuch-Pouchot, M.T.,
386 Bacmann, M., Durif, A. and Wolfers, P. (1983) Etude de la structure et des conditions de
387 stabilite d'un nouvel arseniure de fer: Fe₁₂As₅. *Materials Research Bulletin*, 18, 473-480.

388 Malvin, D.J., Wang, D. and Wasson, J.T. (1984) Chemical classification of iron meteorites—X.
389 Multielement studies of 43 irons, resolution of group IIIE from IIIAB, and evaluation of
390 Cu as a taxonomic parameter. *Geochimica et Cosmochimica Acta*, 48, 785–804.

391 Masters, G. and Gubbins, D. (2003) On the resolution of density within the Earth. *Physics of the*
392 *Earth and Planetary Interiors*, 140, 159–167.

393 McDonough, W.F. and Sun, S.S. (1995) The composition of the Earth. *Chemical geology*, 120,
394 223–253.

395 McDonough, W.F., (2003) 2.15–Compositional model for the earth’s core. *Treatise on*
396 *Geochemistry*, 547–568.

397 Momma, K. and Izumi, F. (2011) VESTA 3 for three-dimensional visualization of crystal,
398 volumetric and morphology data. *Journal of applied crystallography*, 44, 1272–1276.

399 Morard, G., Andrault, D., Guignot, N., Sanloup, C., Mezouar, M., Petitgirard, S. and Fiquet, G.
400 (2008). In situ determination of Fe–Fe₃S phase diagram and liquid structural properties
401 up to 65 GPa. *Earth and Planetary Science Letters*, 620–626.

402 Mori, Y., Ozawa, H., Hirose, K., Sinmyo, R., Tateno, S., Morard, G. and Ohishi, Y. (2017)
403 Melting experiments on Fe–Fe₃S system to 254 GPa. *Earth and Planetary Science Letters*,
404 464 135–141.

405 Murthy, V.R. and Hall, H.T. (1970) The chemical composition of the earth's core: Possibility of
406 sulfur in the core. *Physics of the Earth and Planetary Interiors*, 2, 276–282.

407 Nimmo, F. (2015) Thermal and compositional evolution of the core. In *Core Dynamics* (Ed.
408 Peter Olsen). Vol. 8 *Treatise on Geophysics*, (Exec. Eds. G. Schubert), 217–241.

409 Okada, A., Kobayashi, K., Ito, T. and Sakurai, T. (1991) Structure of synthetic perryite,
410 (Ni, Fe)₈(Si, P)₃. *Acta Crystallographica Section C: Crystal Structure Communications*,
411 47, 1358–1361.

412 Oryshchyn, S., Babizhetskyy, V., Zhak, O., Stoyko, S., Guérin, R., and Simon, A. (2011) Crystal
413 structure of HT-Ni₅P₂ and reinvestigation of isotypic Ni₅As₂. *Intermetallics*, 19,
414 1041–1046.

415 Ozawa, H., Hirose, K., Suzuki, T., Ohishi, Y. and Hirao, N. (2013) Decomposition of Fe₃S
416 above 250 GPa. *Geophysical research letters*, 40, 4845–4849.

417 Prakapenka, V.B., Kubo, A., Kuznetsov, A., Laskin, A., Shkurikhin, O., Dera, P., Rivers, M. L.
418 and Sutton, S.R. (2008) Advanced flat top laser heating system for high pressure research
419 at GSECARS: application to the melting behavior of germanium. *High Pressure*
420 *Research*, 28, 225–235.

421 Prescher, C., and Prakapenka, V.B. (2015) DIOPTAS: a program for reduction of two
422 dimensional X-ray diffraction and data exploration. *High Pressure Research*, 35(3), 223–
423 230.

424 Ricard, Y., Šrámek, O. and Dubuffet, F. (2009) A multi-phase model of runaway core–mantle
425 segregation in planetary embryos. *Earth and Planetary Science Letters*, 284, 144–150.

426 Rigaku Oxford Diffraction (2018) CrysAlisPRO software system, ver. 1.171.39.44a Rigaku
427 Corporation, Oxford, U.K.

428 Ringwood, A.E. (1966) The chemical composition and origin of the Earth. *Advances in earth*
429 *science*, 65, 287.

430 Rubie, D.C., Frost, D.J., Mann, U., Asahara, Y., Nimmo, F., Tsuno, K., Kegler, P., Holzheid, A.
431 and Palme, H. (2011) Heterogeneous accretion, composition and core–mantle
432 differentiation of the Earth. *Earth and Planetary Science Letters*, 301, 31–42.

433 Rundqvist, S. (1960) The structures of Co₂P, Ru₂P and related phases. *Acta Chemica*
434 *Scandinavica*, 14, 1961–1979.

435 Rundqvist, S. and Jellinek, F. (1959) The structures of $\text{Ni}_6\text{Si}_2\text{B}$, Fe_2P and some related phases.
436 *Acta Chemica Scandinavica*, 13, 425–432.

437 Saini, G.S., Calvert, L.D., and Taylor, J.B. (1964). Compounds of the type M_5X_2 : Pd_5As_2 , Ni_5Si_2 ,
438 and Ni_5P_2 . *Canadian Journal of Chemistry*, 42, 1511–1517.

439 Scott, E.R. and Wasson, J.T. (1975) Classification and properties of iron meteorites. *Reviews of*
440 *Geophysics*, 13, 527–546.

441 Seagle, C.T., Campbell, A.J., Heinz, D.L., Shen, G. and Prakapenka, V.B. (2006) Thermal
442 equation of state of Fe_3S and implications for sulfur in Earth's core. *Journal of Geophysical*
443 *Research: Solid Earth*, 111.

444 Shannon, M.C. and Agee, C.B. (1996) High pressure constraints on percolative core formation.
445 *Geophysical Research Letters*, 23, 2717–2720.

446 Sheldrick, G.M. (2015b) Crystal structure refinement with SHELXL. *Acta Crystallographica*
447 *Section C: Structural Chemistry*, 71, 3–8.

448 Stevenson, D.J. (1981). Models of the Earth's core. *Science*, 214, 611–619.

449 Stevenson, D.J. (1988) Fluid dynamics of core formation. In *Topical Conference Origin of the*
450 *Earth* (Vol. 681, p. 87).

451 Tateno, S., Ozawa, H., Hirose, K., Suzuki, T., I-Kawaguchi, S., and Hirao, N. (2019) Fe_2S : the
452 most Fe-rich iron sulfide at the Earth's inner core pressures. *Geophysical Research*
453 *Letters*, 46, 11,944–11,949.

454 Thompson, S., Komabayashi, T., Breton, H., Suehiro, S., Glazyrin, K., Pakhomova, A. and
455 Ohishi, Y. (2020) Compression experiments to 126 GPa and 2500 K and thermal
456 equation of state of Fe_3S : Implications for sulphur in the Earth's core. *Earth and Planetary*
457 *Science Letters*, 534, 116080.

458 Wasson, J.T. and Wai, C.M. (1970) Composition of the metal, schreibersite and perryite of
459 enstatite achondrites and the origin of enstatite chondrites and achondrites. *Geochimica et*
460 *Cosmochimica Acta*, 34, 169-184.

461 Yoshino, T., Walter, M.J. and Katsura, T. (2003) Core formation in planetesimals triggered by
462 permeable flow. *Nature*, 422, 154–157.

463 Yokoo, S., Hirose, K., Sinmyo, R. and Tagawa, S. (2019) Melting experiments on liquidus phase
464 relations in the Fe-S-O ternary system under core pressures. *Geophysical research letters*,
465 46, 5137–5145.

466 Zurkowski, C.C., Lavina, B., Chariton, S., Tkachev, S., Prakapenka V.B. and Campbell A.J.,
467 *in press*. The crystal structure of Fe_2S at 90 GPa based on single-crystal X-ray diffraction
468 techniques. *American Mineralogist*, <https://doi.org/10.2138/am-2022-7973>

469 Zurkowski, C. C., Lavina, B., Brauser, N. M., Davis, A. H., Chariton, S., Tkachev, S.,
470 Greenberg, E., Prakapenka, V. B., and Campbell, A. J., *in press*. Pressure-induced C23-
471 C37 transition and compression behavior of orthorhombic Fe_2S to Earth's core pressures
472 and high temperatures. <https://doi.org/10.2138/am-2022-8187>

473

474

475 **Fe₅S₂ identified as a host for sulfur in Earth's core**

476 **Claire C. Zurkowski^a †, Barbara Lavina^{b,c}, Abigail Case^a, Kellie Swadba^a, Stella Chariton^b,**
477 **Vitali B. Prakapenka^b, Andrew J. Campbell^a**

478
479 ^aThe University of Chicago, Department of the Geophysical Sciences, 5734 S Ellis Ave, Chicago, IL 60637, USA

480 ^bCenter for Advanced Radiation Sources, The University of Chicago, 9700 South Cass Avenue, Lemont, IL 60439,
481 USA

482 ^cX-ray Science Division, Advanced Photon Source, Argonne National Laboratory, Lemont, IL 60439, USA

483 [†]Now at Earth and Planets Laboratory, Carnegie Institution for Science, 5251 Broad Branch Road, NW,
484 Washington, DC 20015, USA

485

486

487

Corresponding Author: Claire Zurkowski, czurkowski@carnegiescience.edu

488 **Supplementary Information**

489 The Supplementary Information includes:

- 490 ➤ Supplementary Information Text
- 491 ➤ Table S1
- 492 ➤ Table S2
- 493 ➤ Table S3
- 494 ➤ Table S4
- 495 ➤ Figure S1
- 496 ➤ Figure S2
- 497 ➤ Figure S3
- 498 ➤ Figure S4
- 499 ➤ Supplementary Information References

500

501

502

503

504

505

506

507

508

509 **Supplementary Information Text**

510 *Synthesis of Fe₅S₂ to 200 GPa*

511 Fe₅S₂ was synthesized between 119(2) and 193(4) GPa with heating to temperatures
512 between 2400–3300 K. The formation of Fe₅S₂ phase was first recognized in the diffraction
513 patterns by the onset of diffuse streaks and sets of closely spaced reciprocal nodes in the powder
514 diffraction images, suggesting a complex atomic arrangement (Figure 1, S1). With sustained
515 high temperatures in the samples loaded in more hydrostatic pressure media (e.g. KCl vs. SiO₂),
516 large grain growth (3 – 6 μm) was observed and the diffuse streaks became less apparent. Further
517 experiments are required to assess the role of hydrostaticity, kinetics, pressure, and temperature
518 on the disorder of this phase.

519 Recrystallization of hcp-Fe with the Fe₅S₂ crystallites at high temperatures was observed
520 in all experiments using the Fe₈₀S₂₀ and Fe₆₇S₃₃ starting powders as evidenced by the spotty
521 (100) and (101) hcp-Fe rings in Figure 1a. Fe-recrystallization with this high-temperature Fe-
522 sulfide establishes that the probed sample locations were in a Fe-saturated phase-field (Figure
523 1a) and this phase is important to consider further in the context of Fe-rich planetary cores.

524 Upon temperature quenching, rotational single-crystal X-ray diffraction scans were
525 performed across a 37–60° omega range, depending on the DAC configuration, and grains were
526 indexed in the reciprocal space to a hexagonal unit cell compatible with an Fe₅S₂ volume (Table
527 S1, Figure 1b). Three unit-cell polytypes were observed and indexed in our experiments and are
528 listed in Table S1. All indexed grains exhibit an *a* axial length of ~ 6 Å, while 3 differing *c* axial
529 lengths are observed: ~ 11, 26, and 73 Å. Diffraction mappings show that the polytypism is
530 accompanied by diffuse scattering suggesting positional disorder as the atomic arrangement
531 along the *c* axis configures at high temperatures (Figure S1). Analogous polytypism has also

532 been observed in the transition metal binary phase Pb_5As_2 (Saini et al. 1964). Decreased diffuse
533 scattering from the Fe_5S_2 grains was observed after continued heating in the KCl pressure media,
534 and grains with $a \sim 6 \text{ \AA}$, $c \sim 11 \text{ \AA}$ were indexed, indicating that this configuration is the most
535 positionally ordered arrangement relevant to these high P - T conditions. These measured unit cell
536 parameters are compatible with 6 formula units per cell volume of Fe_5S_2 .

537 The structure of a grain Fe_5S_2 synthesized at 140(2) GPa and 3070(180) K was
538 determined based on 159 observed reflections at these extreme conditions (Table S2).
539 Assessment of the systematic absences for the structure factors reduced for Fe_5S_2 suggests a
540 $P6_3cm$ space group. Structural solution and positional and displacement parameter refinement
541 converged on the Ni_5As_2 structure type (Table S2, 3; Figure 2) (Oryshchyn et al. 2011). The
542 Ni_5As_2 structure is a slight modification of the Pb_5Sb_2 structure (El-Boragy et al. 1970) where the
543 Fe6 site (Table S3) is split about its position and given half occupancy, changing its Wyckoff site
544 from 6c to 12d (Figure 2) (Oryshchyn et al. 2011). This structural modification was initiated
545 based on the large U_{22} parameter observed on the $M6$ site ($M = \text{metal}$) in Ni_5As_2 when
546 anisotropic displacement parameters were refined using a Pb_5As_2 starting model (Figure S2). In
547 the current dataset, a comparably large U_{22} value was observed on the Fe6 site resulting in an
548 oblong displacement ellipse when refining the data against the initial Pb_5As_2 structure model.
549 The Fe6 site was positionally disordered following Oryshchyn et al. (2011), and the resultant R_1
550 value was improved by around $\sim 5\%$, rendering the Ni_5As_2 structure model more compatible with
551 the current Fe_5S_2 data (Table S2). Isotropic displacement parameters showing errors $> 3\sigma$ were
552 fixed to a value equal to approximately the average displacement parameter value for Fe or S
553 (Table S2). The isotropic displacement parameter for the disordered Fe site was also fixed at an
554 average Fe_{Uiso} value (Table S2). The number of reflections collected at these extreme pressures

555 limits the number of statistically meaningful parameters to refine, and fixing displacement
556 parameters to reasonable values precludes overinterpretation of the current dataset. The high
557 isotropic displacement parameter observed on the Fe4 site may represent some vacancies on this
558 site, but the dataset is again deficient to precisely describe the site occupancy.

559 The experimental details for the solution and refinement of Fe₅S₂ to the Ni₅As₂ solution
560 model are provided in Table S2 and the atomic coordinates of Fe₅S₂ synthesized at 140(2) GPa
561 and 3070(180) K are provided in Table S3. In accordance with previous descriptions of related
562 *M₅X₂* transitional-metal binary phases (e.g. (Kjekshus et al. 1973; Oryshchyn et al. 2011), Fe₅S₂
563 can be viewed as an arrangement of 6 Fe sites and 3 S sites with the Fe1, Fe2, Fe4, and Fe6 sites
564 are in 13-fold coordination, the Fe3 and Fe5 sites are in 12-fold coordination, and the S sites are
565 in 10-fold coordination (Figure 2c). The measured bond lengths for the Fe-coordinated polyhedra
566 are provided in Table S4. All sites are coordinated by both Fe and S sites. A CIF file for Fe₅S₂
567 is provided in Appendix A1.

568 Final R₁ values \simeq 10% attest to the less-than ideal quality of the multigrain dataset as a
569 possible result of the 1-2 megabar synthesis conditions and observed *c* axial disorder and
570 stacking complexities in Fe₅S₂ (Table S2). Previous studies of isomorphic Ni₅As₂ and related
571 Pb₅As₂ at ambient conditions have also reported similar quality of refinements despite obtaining
572 significantly more reflections in the absence of a DAC (e.g. Saini et al. 1964; El-Boragy et al.
573 1970; Kjekshus et al. 1973). Notable challenges regarding the refinement of the Fe₅S₂ structure
574 model at these extreme conditions are discussed here and compared with similar difficulties
575 reported in previous characterizations of this structure.

576 Thirteen violations of the *P6₃cm* systematic absence condition: $l = 2n$ for (0*kl*), were
577 flagged during the refinement of Fe₅S₂. The reflections associated with these systematic absence

578 violations were examined in the raw diffraction images and all show low, diffuse intensity.
579 Discrepancy over the presence or absence of weak reflections with $(0kl)$, $l=2n+1$ has been
580 reported in previous investigations of Ni_5As_2 and Pb_5As_2 (e.g. Saini et al. 1964; El-Boragy et al.
581 1970; Kjekshus et al. 1973), suggesting that these studies may have also faced difficulties with
582 space group determination. Observations of these low-intensity reflections may be a result of
583 residual disorder in the stacking arrangement along the c direction, and longer heating cycles
584 may be required for the atoms to arrange into equilibrium positions. It is likewise possible that
585 varying synthesis methods for Ni_5As_2 and Pb_5As_2 in previous ambient condition studies affected
586 the c axial atomic arrangement. Ni_5As_2 and isomorphic Ni_5P_2 also exhibits a homogeneity range
587 of $\sim 71.25 - 72.7$ atomic % As (Kjekshus et al. 1973; Litasov et al., 2019), and slight
588 modifications of this structure based on varying stacking arrangements result in structures such
589 as $\text{Ni}_{31}\text{Si}_{12}$ (Frank and Schubert 1971) and $(\text{Fe, Ni})_8(\text{Si, P})_3$ (perryite) (Okada et al. 1991).
590 Attempts to refine the current Fe-sulfide phase with the $\text{Ni}_{31}\text{Si}_{12}$ or perryite structure models did
591 not improve the refinement results. Based on the presence of disorder, polytypism, anisotropic
592 vibrational motion, and nonstoichiometry in the related M_5X_2 phases, additional nuances to the
593 Fe_5S_2 structure model may be developed in future studies; however, the identification and
594 characterization of the Fe_5S_2 crystal structure determined here to 200 GPa is novel, and the
595 observations and challenges reported in this study align with that of previous analyses of Ni_5As_2
596 and Pb_5Sb_2 that were not limited by microdiffraction in a DAC at extreme conditions.

597

598 *Other sulfides observed during heating to 200 GPa*

599 Three experiments and 7 heating cycles were performed in this study between 100 and
600 200 GPa and to 3400 K, and the X-ray diffraction patterns collected upon heating provide insight

601 into the Fe-rich Fe-S phase relations at outer core pressures and to high temperatures. In each
602 heating experiment, near melting temperatures were targeted and grains of Fe₅S₂ were identified
603 upon quenching. Additional Fe-sulfides were also observed across the thermal gradient of the
604 heated spot, providing information on the lower temperature Fe-saturated phase relations in each
605 heating cycle. Upon quenching from high-temperature synthesis at 119(2) GPa, the other grains
606 in the sample were identified and indexed to a tetragonal cell with $a = 8.094(3)$ Å, $c = 3.990(2)$
607 Å, compatible with 8 formula units of Fe₃S (Table S1). The structure was then solved and refined
608 to the Fe₃P-type structure ($I-4$, $Z = 8$) (referred to herein as $I-4$ Fe₃S) in agreement with previous
609 studies (Fei et al. 2000; Seagle et al. 2006; Morard et al. 2007; Kamada et al. 2010; Kamada et
610 al. 2012; Thompson et al. 2020). The resultant structure model for Fe₃S at these conditions is
611 shown in Figure (3a), a CIF file for Fe₃S is provided in Appendix A2, and the refinement details
612 are given in Table S2. The structure can be viewed as containing 3 tetrahedrally coordinated Fe
613 sites (Blanchard et al. 2008): one Fe-site is coordinated only by S atoms with an average bond
614 length of 2.083(9) Å, another Fe site is coordinated by 3 S atoms and 1 Fe atom with an average
615 bond length of 2.146(8) Å, and the third Fe site is coordinated by 2 S and 2 Fe atoms with an
616 average bond length of 2.137(8) Å (Figure 3). The measured interatomic distances are
617 comparable to reports on other transition metal M_3X structures (e.g. Aronsson 1955; Rundqvist
618 1979).

619 After temperature quenching from 131(2) GPa and 3050(140) K, grains of Fe₃S were not
620 observed across the heated spot. Instead, orthorhombic lattices were also identified with
621 parameters $a = 4.869(2)$ Å, $b = 3.256(2)$ Å, $c = 6.139(2)$ Å, compatible with 4 formula units of
622 Fe₂S. Structural solution and refinement indicate that the Fe₂S grains adopt the $C23$ structure
623 (Co₂P type, $Pnma$, $Z = 4$) in agreement with previous structural analyses at lower pressures

624 (Zurkowski et al. *in press*). Refinement details for the structure model are given in Table S2 and
625 a CIF file for *C23* Fe₂S is provided in Appendix A3. The structure is composed of columns of
626 FeS₄ tetrahedra and columns of FeS₅ square pyramids linked along edges in the *b* direction
627 (Figure 3b). The average Fe–S bond lengths are 2.213(8) Å and 2.011(2) Å in the square
628 pyramids and tetrahedra, respectively. These values are comparable with that observed in *C23*
629 Fe₂S at 90 GPa (Zurkowski et al. *in press*).

630 Upon compression and heating at 140(2) GPa and 3070(180) K, orthorhombic grains
631 were identified in the sample chamber with $a = 4.667(2)$ Å, $3.289(1)$ Å, $6.186(4)$ Å. This unit
632 cell is similar to the *C23* Fe₂S observed at 130 GPa, but exhibits a 4 % contraction of the *a* axial
633 length, a 1% extension of the *b* and *c* axial lengths, and a 2% volume decrease. Structural
634 solution and refinement using the measured structure factors establish that Fe₂S adopts the *C37*
635 structure (Co₂Si-type, *Pnma*, *Z*=4) at these conditions (Figure 3c). A CIF file for *C37* Fe₂S is
636 provided in Appendix A4 and the analysis details are given in Table S2. In agreement with the
637 proposed *C23*–*C37* Fe₂S phase transition around 140 GPa that is accompanied 1.6% volume
638 decrease (Zurkowski et al., *in press*), this work confirms that the *C23*–*C37* transition in Fe₂S
639 occurs between 130 and 140 GPa with a similar volume change. Inherent to the *C23*–*C37*
640 transition is coordination change from the 4-fold Fe1 coordination polyhedra in the *C23* structure
641 to the 5-fold dipyramid polyhedra in the *C37* structure (Figure 3b, c). Comparing the *C23* and
642 *C37* structure models determined at 130 and 140 GPa, respectively, a 10% contraction of the
643 interatomic distance involved in the coordination change is observed (Figure S3). The average
644 Fe–S bond lengths measured in *C37* Fe₂S are 2.196(2) Å and 2.165(3) Å in the square pyramids
645 and dipyramids, respectively. These values are comparable with *C23* Fe₂S.

646

647 *Fe-rich sulfide phase relations at core-mantle boundary pressures*

648 The presented single-crystal derived structures of Fe_5S_2 , Fe_3S , $C23 \text{Fe}_2\text{S}$ and $C37 \text{Fe}_2\text{S}$
649 were then used to inform the changes in diffraction patterns collected during heating between
650 110 and 200 GPa and to ~ 3300 K. Beginning at 112 GPa, diffraction signal from $C23 \text{Fe}_2\text{S}$
651 coexisting with Fe was first identified upon heating of the $\text{Fe}_{80}\text{S}_{20}$ starting material to ~ 2000 K.
652 With continued heating, peaks associated with tetragonal Fe_3S were observed over a limited
653 temperature range ($\lesssim 2400$ K) until diffuse scattering signal and Bragg reflections from Fe_5S_2
654 first appeared. Crystallization of the Fe_5S_2 grains with iron occurred with continued heating to
655 119(2) GPa and 2840(180) K. Upon heating beginning at 120 GPa, $C23 \text{Fe}_2\text{S}$ was observed
656 coexisting with Fe to 122(1) GPa and 2290(120) K, above which the onset of diffraction from
657 the Fe_5S_2 phase was identified and Fe_5S_2 crystallites formed coexisting with hcp-Fe to 131(2)
658 GPa and 3050(140) K. $I-4 \text{Fe}_3\text{S}$ was not observed. With continued heating cycles between 133(1)
659 GPa and 194(2) GPa and up to 3300 K, $C37 \text{Fe}_2\text{S}$ coexists with Fe at moderate temperatures and
660 a phase transition to Fe_5S_2 occurs at high temperatures. A phase diagram satisfying these
661 observations is proposed in Figure 4, and integrated XRD patterns for the heating cycles at
662 119(2) and 184(3) GPa and to 3300 K are shown in Figure S4 to demonstrate the identification
663 of $C23 \text{Fe}_2\text{S}$, Fe_3S , $C37 \text{Fe}_2\text{S}$, and Fe_5S_2 coexisting with hcp-Fe. The peak intensities from the
664 Fe_5S_2 lattices vary during heating up at high temperatures as a result of disorder, polytypism, and
665 the formation of large crystallites at high temperatures (Figure 1, S1). These structural
666 complexities render the powder diffraction patterns difficult to characterize without
667 incorporating single-crystal XRD techniques.

668

669 *Discrepancies among the current and previous studies*

670 Transitional metal binary compounds with metal-to-nonmetal ratios ranging from 2.33–
671 2.66 (~70–73 atm% metal) predominantly adopt complex trigonal or hexagonal structures with
672 considerable metal-metal bonding (Chen and Whitmire 2018 and references therein). Our
673 observations of the disorder, polytypism, and complex coordination environments inherent to
674 Fe_5S_2 demonstrate that it aligns with this systematic characterization. Interestingly, the Fe_5S_2
675 atomic arrangement is thermodynamically favored at the extreme conditions of Earth's outer
676 core over that of *I*-4 Fe_3S . These results are contrary to previous reports of Fe_3S stability on to
677 high temperatures in Fe-rich systems to 250 GPa (Kamada et al. 2010; Kamada et al. 2012;
678 Ozawa et al. 2013; Mori et al. 2017). Few lines of reasoning may account for these
679 discrepancies. Interpretation of Fe_5S_2 in the integrated powder diffraction patterns is difficult due
680 to the variation in diffraction signal obtained from the Fe_5S_2 polytypes and the low intensity
681 scattering from the disordered sites during its formation. Fe_5S_2 also forms large crystallites,
682 limiting the orientations of the phase and rendering indexation of all diffraction angles for Fe_5S_2
683 quite challenging without rotating the sample. The implementation of single-crystal X-ray
684 diffraction techniques at high pressures was critical in the current study to accurately
685 characterize the hexagonal unit cell geometry and complex structure of the Ni_5As_2 -like Fe_5S_2 .

686 Several studies have also reported chemically analyzed Fe_3S grains in samples recovered
687 from high temperatures in the 200–250 GPa range (Mori et al. 2017; Yokoo et al. 2019; Ozawa
688 et al. 2013), but the difference in Fe content between Fe_3S and Fe_5S_2 may be as few as 3%. This
689 value is generally within 3 sigma of the atomic percent error reported for chemical analyses of
690 samples recovered from these extreme conditions, posing another challenge for distinguishing
691 between the synthesis of Fe_3S and Fe_5S_2 . Furthermore, based on characterizations of the

692 isomorphous Ni_5As_2 and Ni_5P_2 , these structures exhibit a homogeneity range with up to ~73 atm%
693 metal (Kjekshus et al. 1973; Litasov et al., 2019). For example, TEM analysis of a Fe–S sample
694 recovered from 236 GPa and 2980 K reveals sulfide grains with on average ~73 atm% Fe
695 (Ozawa et al. 2013). This value is within 0.3–1.25 atomic percent of the possible range of Fe_5S_2
696 stoichiometries and 2 atomic percent less than an Fe_3S composition. The results from this
697 previous work as well as other chemical analyses of samples recovered from outer core pressures
698 and high temperatures therefore do not contradict the current results (Mori et al. 2017; Yokoo et
699 al. 2019; Ozawa et al. 2013) and may reveal a previous misinterpretation of Fe_5S_2 as Fe_3S based
700 on measured chemistries.

701

702

703 **Table S1.** Unit cell parameters of Fe₅S₂, Fe₃S, and Fe₂S measured upon quenching from high *P*-
704 *T* synthesis in this study. Each cell was indexed in the reciprocal space, and the DAC opening,
705 and number of reflections obtained for each lattice are listed. For select experiments, high-
706 temperature synthesis was conducted without collecting X-ray diffraction data, and the synthesis
707 conditions for these experiments are listed as “high T, not measured.”

Sample name	Starting		Phase	Room temperature collection							Synthesis conditions	
	material	medium		P	<i>a</i>	<i>b</i>	<i>c</i>	V	DAC opening	no. of reflections	<i>P</i>	<i>T</i>
				GPa	Å	Å	Å	Å ³	(°)		GPa	K
C140_P2_map25	Fe80S20	KCl	Fe5S2	105(2)	6.020(4)		11.204(7)	351.6(5)	60	290	119(2)	2840(140)
C140_P2_map31	Fe80S20	KCl	Fe5S2	105(2)	6.050(2)		73.0(2)	2313(1)	60	134	119(2)	2840(140)
C140_P4_map10	Fe80S20	KCl	Fe5S2	118(1)	5.983(3)		11.078(6)	343.4(4)	60	489	140(2)	3070(180)
C140_P4_map14	Fe80S20	KCl	Fe5S2	118(1)	5.979(2)		11.084(4)	343.2(3)	60	379	140(2)	3070(180)
C140_P4_map14	Fe80S20	KCl	Fe5S2	118(1)	5.973(1)		11.094(2)	342.8(1)	60	276	140(2)	3070(180)
C129_P140_map71	Fe67S33	SiO2	Fe5S2	136.4(5)	5.957(4)		71.89(4)	2209(3)	34	84	159(2)	3230(150)
C129_P150_map9	Fe67S33	SiO2	Fe5S2	144.2(8)	5.939(3)		25.99(6)	794(2)	34	76	high T, not measured	
C129_P150_map9	Fe67S33	SiO2	Fe5S2	144.2(8)	5.923(1)		26.004(6)	789.9(3)	34	146	high T, not measured	
C137_P1_map25	Fe80S20	SiO2	Fe5S2	159(1)	5.890(3)		25.837(7)	776.2(5)	40	108	184(3)	3250(260)
C137_P1_map25	Fe80S20	SiO2	Fe5S2	159(1)	5.880(1)		25.789(3)	772.0(2)	40	108	184(3)	3250(260)
C137_P1_map25	Fe80S20	SiO2	Fe5S2	159(1)	5.876(2)		25.884(8)	774.0(4)	40	116	184(3)	3250(260)
C137_P1_map25	Fe80S20	SiO2	Fe5S2	159(1)	5.883(3)		25.85(1)	774.6(7)	40	126	184(3)	3250(260)
C137_P1	Fe80S20	SiO2	Fe5S2	159(1)	5.897(3)		25.90(1)	775.1(6)	40	116	184(3)	3250(260)
C137_P1	Fe80S20	SiO2	Fe5S2	159(1)	5.878(1)		25.784(3)	771.6(2)	40	149	184(3)	3250(260)
C137_P2_34	Fe80S20	SiO2	Fe5S2	179(1)	5.8400(7)		25.583(2)	755.7(1)	40	189	193(4)	3010(160)
C140_P1_map	Fe80S20	KCl	Fe3S	100(1)	8.156(3)		4.025(3)	267.8(3)	60	416	high T, not measured	
C140_P2_map25	Fe80S20	KCl	Fe3S	105(2)	8.094(3)		3.990(2)	261.4(2)	60	296	119(2)	2840(140)
C140_P3_map6	Fe80S20	KCl	C23Fe2S	111(1)	4.869(2)	3.256(2)	6.139(2)	97.3(1)	60	227	131(2)	3050(140)
C140_P4_map10	Fe80S20	KCl	C37Fe2S	118(1)	4.677(2)	3.289(1)	6.186(4)	95.18(9)	60	188	140(2)	3070(180)

708
709
710
711
712
713
714
715
716
717
718
719
720
721
722
723
724

725 **Table S2.** Select experimental details for crystal structure synthesis and analysis of Fe₅S₂, Fe₃S,
 726 and the Fe₂S polymorphs.

Phase	Fe ₅ S ₂	Fe ₃ S	C23 Fe ₂ S	C37 Fe ₂ S
Sample Name	C140_P4_map10	C140_P2_map25	C140_P3_map6	C140_P4_map10
Synthesis				
Pressure (GPa)	140(2)	119(2)	131(2)	140(2)
Synthesis Temperature (K)	3070(180)	2840(140)	2050(140)	3070(180)
Symmetry	Hexagonal, <i>P6(3)cm</i> , Z=6	Tetragonal, <i>I-4</i> , Z=8	Orthorhombic, <i>Pnma</i> , Z = 4	Orthorhombic, <i>Pnma</i> , Z = 4
<i>a</i> (Å)	5.979(2)	8.094(3)	4.869(3)	4.677(2)
<i>b</i> (Å)			3.256(4)	3.289(1)
<i>c</i> (Å)	11.087(6)	3.990(2)	6.139(2)	6.186(4)
<i>V</i> (Å ³)	343.2(3)	226.4(2)	97.3(1)	95.18(9)
Reduction				
No. of measured, independent and observed [<i>I</i> > 2σ(<i>I</i>)] reflections	396, 309, 157	332, 314, 219	227, 208, 112	188, 158, 105
<i>R</i> _{int} , <i>R</i> _{sigma}	0.092, 0.062	0.053, 0.072	0.012, 0.016	0.009, 0.014
Refinement				
<i>R</i> [<i>F</i> ² > 2σ(<i>F</i> ²)], <i>wR</i> (<i>F</i> ²), <i>S</i>	0.098, 0.255, 1.12	0.067, 0.164, 1.05	0.053, 0.149, 1.21	0.047, 0.139, 1.22
No. of reflections	156	219	112	105
No. of parameters	21	17	10	10
Δρ _{max} , Δρ _{min} (e Å ⁻³)	2.14, -2.18	1.92, -1.68	1.86, -2.02	1.91, -2.21

727
 728
 729
 730
 731
 732

733 **Table S3.** Atomic coordinates of the Fe₅S₂ refinement model for the data collected at 140(2) GPa
 734 and quenched from 3070(180) K.

Wycoff site	ATOM	x	y	z	Uiso
2a	Fe1	0	0	0.963	0.021
	error			0.003	0.005
4b	Fe2	1/3	2/3	0.089	0.046
	error			0.003	0.005
6c	Fe3	0.259	0	0.126	0.021
	error	0.002		0.001	
6c	Fe4	0.613	0	0.222	0.021
	error	0.002		0.001	0.003
6c	Fe5	0.284	0	0.330	0.027
	error	0.002		0.001	0.003
12d	Fe6*	0.651	0.056	0.426	0.021
	error	0.003	0.003	0.002	
2a	S1	0	0	0.220	0.026
	error			0.004	
4b	S2	1/3	2/3	0.299	0.026
	error			0.002	
6c	S3	0.673	0	0.030	0.026
	error	0.005		0.003	

*indicates half occupancy

735
 736
 737
 738
 739
 740
 741
 742
 743
 744
 745
 746
 747

748 **Table S4.** Selected interatomic distances for the Fe sites measured in Fe₅S₂ at 140 GPa.

Atom	bonded to	#	distance (Å)
Fe1	-Fe3	3	2.39(2)
	-Fe5	3	2.22(3)
	-Fe6	3	2.313(17)
	-S1	1	2.66(8)
	-S4	3	2.09(3)
Fe2	-Fe3	3	2.275(3)
	-Fe4	3	2.375(16)
	-Fe6	3	2.40(3)
	-S3	1	2.36(4)
	-S4	3	2.108(13)
Fe3	-Fe1	1	2.39(2)
	-Fe2	2	2.275(8)
	-Fe4	3	2.350(15)
	-Fe5	1	2.30(3)
	-Fe6	1	2.307(17)
	-S1	1	1.90(4)
	-S4	3	2.68(3)
Fe4	-Fe2	2	2.375(16)
	-Fe3	3	2.320(11)
	-Fe5	3	2.416(14)
	-Fe6	1	2.303(17)
	-S1	1	2.326(11)
	-S3	2	2.044(16)
	-S4	1	2.10(3)
Fe5	-Fe1	1	2.22(3)
	-Fe3	1	2.30(3)
	-Fe4	3	2.416(14)
	-Fe6	3	2.135(15)
	-S1	1	2.09(5)
	-S3	2	2.184(10)
	-S4	1	2.27(3)
Fe6	-Fe1	1	2.313(17)
	-Fe2	2	2.40(3)
	-Fe3	1	2.307(17)
	-Fe4	1	2.303(17)
	-Fe5	3	2.135(15)
	-S3	2	2.15(3)
	-S4	3	2.17(3)

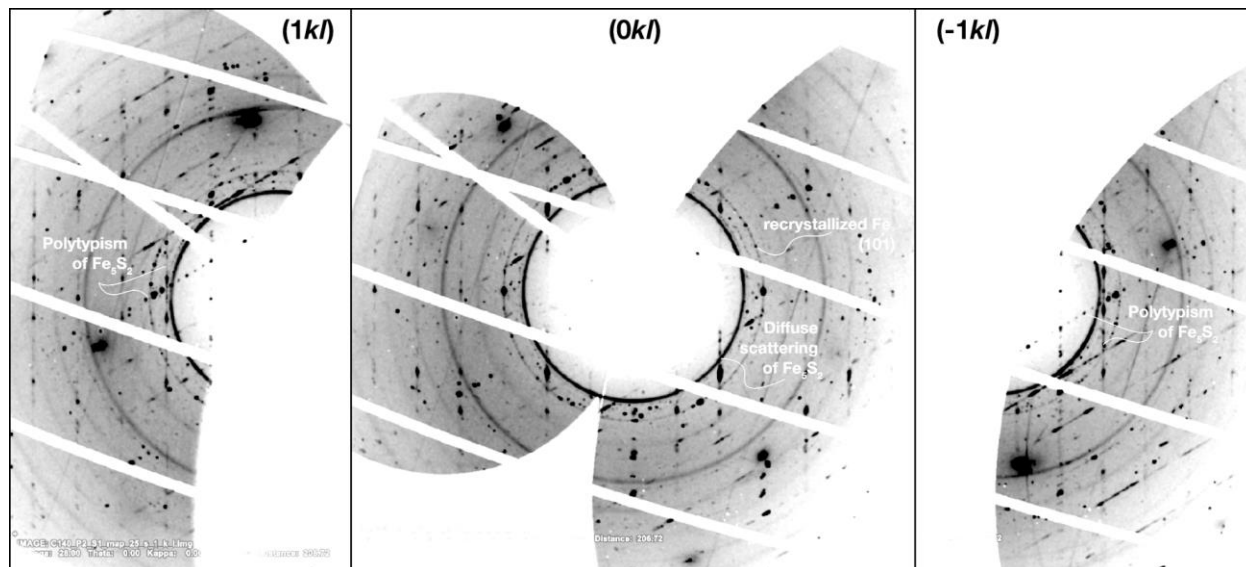
749

750

751

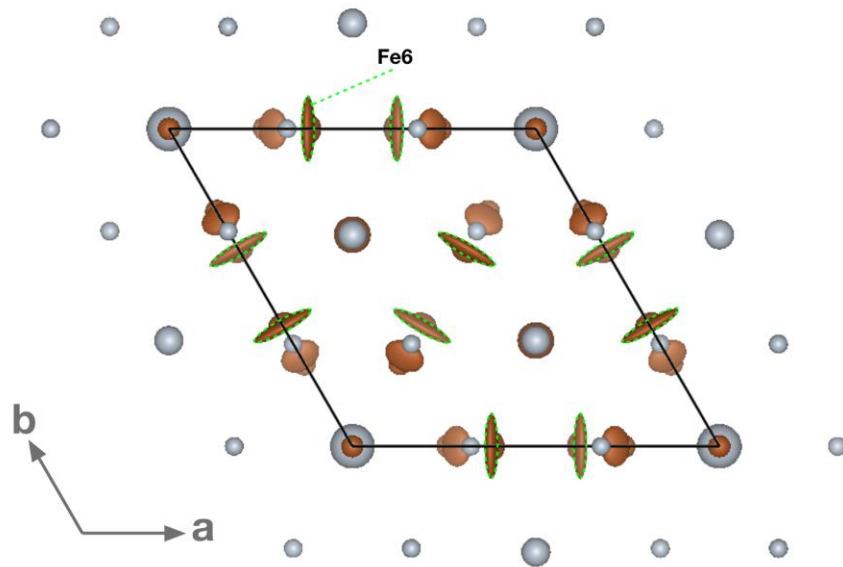
752

753 **Figure S1.** Unwarped diffraction mappings of the $(1kl)$, $(0kl)$, and $(-1kl)$ directions for an Fe_5S_2
754 crystallite exemplifying the diffuse scattering signal collected at 119(2) and 2840(180) K. The
755 $(1kl)$ and $(-1kl)$ mappings also show the presence of a polytype with more closely spaced
756 reflections oriented $\sim 51^\circ$ from the mapped crystallite.



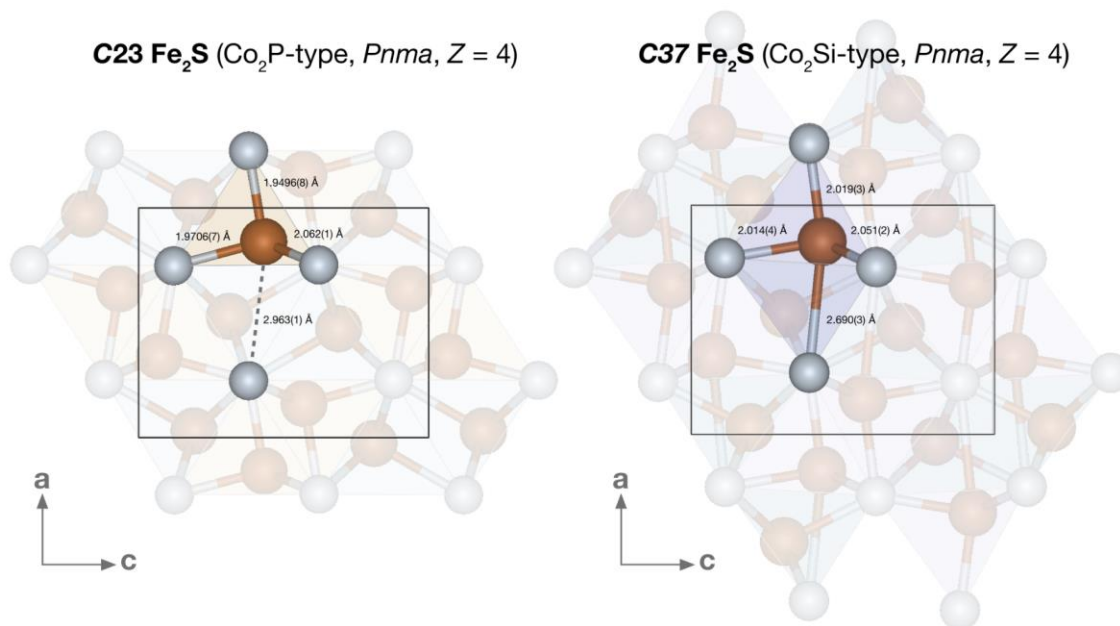
757
758
759
760
761
762
763

764 **Figure S2.** Fe_5As_2 structure model shown with anisotropic displacement ellipsoids using the
765 starting Pb_5As_2 structure model. In accordance with the Ni_5As_2 structural characterization
766 (Oryshchyn et al. 2011), these sites were disordered about their position and ascribed half
767 occupancy.

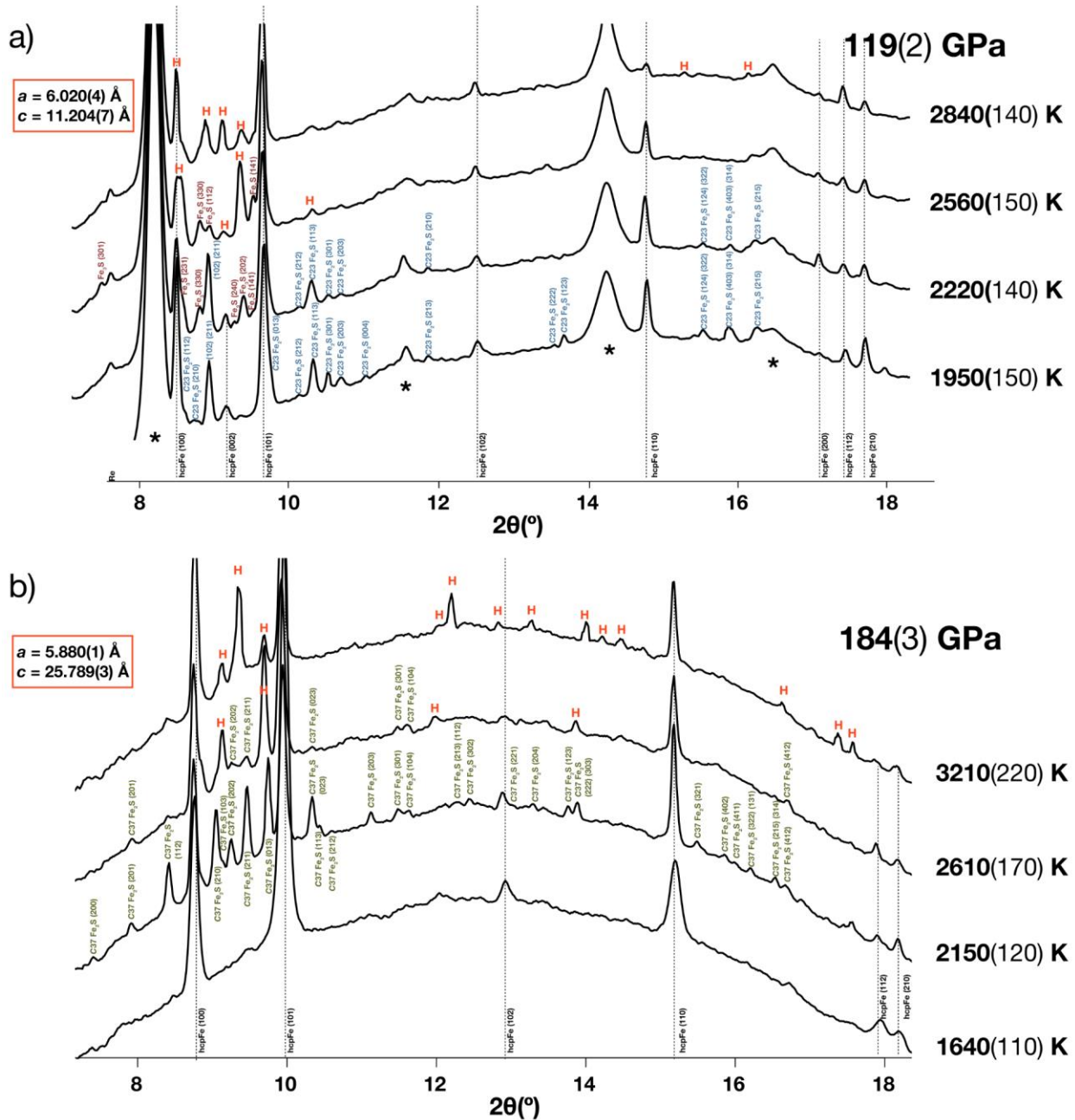


768
769
770
771
772
773
774
775
776
777
778
779
780
781
782
783
784
785
786

787 **Figure S3.** Comparison of the *C23* and *C37* structure models refined at 130 and 140 GPa,
788 respectively. In the *C23* Fe₂S structure, the next nearest sulfur site to the Fe1 tetrahedral site is at
789 a 2.963(1) Å distance at 130 GPa (dotted line). A 10% contraction of this interatomic distance
790 and a coordination change is observed in the formation of *C37* Fe₂S at 140 GPa (right).
791



811 **Figure S4.** X-ray diffraction patterns collected upon heating in an Fe₈₀S₂₀ starting composition at
 812 a) 119(2) GPa and b) 184(3) GPa. The miller indices for C23 Fe₂S (blue), Fe₃S (burgundy), and
 813 C37 Fe₂S (green) are provided, and the red “H” symbols represent the observations of the
 814 formation of Fe₅S₂. The growth of large crystallites, along with the disorder and polytypism of
 815 this phase make for challenging powder diffraction indexing, but the lattice parameters of Fe₅S₂
 816 indexed in the reciprocal space after quenching from these high *P-T* conditions are provided.



817
 818

819

820 **Supplementary Information References**

- 821 Aronsson, B. (1955) The crystal structure of Ni₃P. (Fe₃P-Type). *Acta Chemica Scandinavica*, 9,
822 137-140.
- 823 Blanchard, P.E., Grosvenor, A.P., Cavell, R.G. and Mar, A. (2008) X-ray Photoelectron and
824 Absorption Spectroscopy of Metal-Rich Phosphides M₂P and M₃P (M=
825 Cr– Ni). *Chemistry of Materials*, 20, 7081-7088.
- 826 Chen, J.H. and Whitmire, K.H. (2018) A structural survey of the binary transition metal
827 phosphides and arsenides of the d-block elements. *Coordination Chemistry Reviews*, 355,
828 271–327.
- 829 El-Boragy, M., Bhan, S. and Schubert, K. (1970) Kristallstruktur von Pd₅Sb₂ und Ni₅As₂ und
830 einigen varianten. *Journal of the Less Common Metals*, 22, 445–458.
- 831 Fei, Y., Li, J., Bertka, C.M. and Prewitt, C.T. (2000) Structure type and bulk modulus of Fe₃S, a
832 new iron-sulfur compound. *American Mineralogist*, 85, 1830–1833.
- 833 Frank, K. and Schubert, K. (1971) Kristallstruktur von Ni₃₁Si₁₂. *Acta Crystallographica Section*
834 *B: Structural Crystallography and Crystal Chemistry*, 27, 916–920.
- 835 Kamada, S., Terasaki, H., Ohtani, E., Sakai, T., Kikegawa, T., Ohishi, Y., Hirao, N., Sata, N. and
836 Kondo, T. (2010) Phase relationships of the Fe–FeS system in conditions up to the
837 Earth's outer core. *Earth and Planetary Science Letters*, 294, 94–100.
- 838 Kamada, S., Ohtani, E., Terasaki, H., Sakai, T., Miyahara, M., Ohishi, Y. and Hirao, N. (2012)
839 Melting relationships in the Fe–Fe₃S system up to the outer core conditions. *Earth and*
840 *Planetary Science Letters*, 359, 26–33.
- 841 Kjekshus, A., Skaug, K.E., Hebrew, C., Van Buren, C.T., Klæboe, P. and Swahn, C.G. (1973).
842 On the crystal structure of Ni₅As₂. *Acta Chem. Scand.*, 27, 582–588.
- 843 Litasov, K.D., Shatskiy, A.F., Minin, D.A., Kuper, K.E. and Ohfuji, H. (2019). The Ni–Ni₂P
844 phase diagram at 6 GPa with implication to meteorites and super-reduced terrestrial
845 rocks. *High Pressure Research*, 39, 561–578.
- 846 Morard, G., Andrault, D., Guignot, N., Sanloup, C., Mezouar, M., Petitgirard, S. and Fiquet, G.
847 (2008). In situ determination of Fe–Fe₃S phase diagram and liquid structural properties
848 up to 65 GPa. *Earth and Planetary Science Letters*, 620–626.
- 849 Mori, Y., Ozawa, H., Hirose, K., Sinmyo, R., Tateno, S., Morard, G. and Ohishi, Y. (2017)
850 Melting experiments on Fe–Fe₃S system to 254 GPa. *Earth and Planetary Science Letters*,
851 464 135–141.
- 852 Okada, A., Kobayashi, K., Ito, T. and Sakurai, T. (1991) Structure of synthetic perryite,
853 (Ni, Fe)₈(Si, P)₃. *Acta Crystallographica Section C: Crystal Structure Communications*,
854 47, 1358–1361.
- 855 Oryshchyn, S., Babizhetskyy, V., Zhak, O., Stoyko, S., Guérin, R., and Simon, A. (2011) Crystal
856 structure of HT-Ni₅P₂ and reinvestigation of isotypic Ni₅As₂. *Intermetallics*, 19,
857 1041–1046.
- 858 Ozawa, H., Hirose, K., Suzuki, T., Ohishi, Y. and Hirao, N. (2013) Decomposition of Fe₃S
859 above 250 GPa. *Geophysical research letters*, 40, 4845–4849.

860 Rundqvist, S. (1960) The structures of Co_2P , Ru_2P and related phases. *Acta Chemica*
861 *Scandinavica*, 14, 1961–1979.

862 Rundqvist, S. and Jellinek, F. (1959) The structures of $\text{Ni}_6\text{Si}_2\text{B}$, Fe_2P and some related phases.
863 *Acta Chemica Scandinavica*, 13, 425–432.

864 Saini, G.S., Calvert, L.D., and Taylor, J.B. (1964). Compounds of the type M_5X_2 : Pd_5As_2 , Ni_5Si_2 ,
865 and Ni_5P_2 . *Canadian Journal of Chemistry*, 42, 1511–1517.

866 Seagle, C.T., Campbell, A.J., Heinz, D.L., Shen, G. and Prakapenka, V.B. (2006) Thermal
867 equation of state of Fe_3S and implications for sulfur in Earth's core. *Journal of Geophysical*
868 *Research: Solid Earth*, 111.

869 Thompson, S., Komabayashi, T., Breton, H., Suehiro, S., Glazyrin, K., Pakhomova, A. and
870 Ohishi, Y. (2020) Compression experiments to 126 GPa and 2500 K and thermal
871 equation of state of Fe_3S : Implications for sulphur in the Earth's core. *Earth and Planetary*
872 *Science Letters*, 534, 116080.

873 Yokoo, S., Hirose, K., Sinmyo, R. and Tagawa, S. (2019) Melting experiments on liquidus phase
874 relations in the Fe-S-O ternary system under core pressures. *Geophysical research letters*,
875 46, 5137–5145.

876 Zurkowski, C.C., Lavina, B., Chariton, S., Tkachev, S., Prakapenka V.B. and Campbell A.J.,
877 *in press*. The crystal structure of Fe_2S at 90 GPa based on single-crystal X-ray diffraction
878 techniques. *American Mineralogist*, <https://doi.org/10.2138/am-2022-7973>

879 Zurkowski, C. C., Lavina, B., Brauser, N. M., Davis, A. H., Chariton, S., Tkachev, S.,
880 Greenberg, E., Prakapenka, V. B., and Campbell, A. J., *in press*. Pressure-induced C23-
881 C37 transition and compression behavior of orthorhombic Fe_2S to Earth's core pressures
882 and high temperatures. <https://doi.org/10.2138/am-2022-8187>
883
884